Synthesis and characterization of Ammonium Hexachlorostannate perovskite and its application as cathode material in Lithium-ion batteries

Alfredo Romero-Contreras
Universidad Autónoma de Nuevo León
Thelma Serrano-Quezada
Universidad Autónoma de Nuevo León
Nora Aleyda Garcia-Gomez
Universidad Autónoma de Nuevo León
Salome Maribel de la Parra-Arcinega
Universidad Autónoma de Nuevo León
Eduardo Maximiano Sanchez-Cervantes
eduardo.sanchezcv@uanl.edu.mx
Universidad Autónoma de Nuevo León

Research Article

Keywords:

Posted Date: November 28th, 2024

DOI: https://doi.org/10.21203/rs.3.rs-5411702/v1

Additional Declarations: No competing interests reported.

Abstract

One of the most interesting topics in energy storage area is the use of organic–inorganic hybrids materials due to the possibility of integrating properties of inorganic and organic molecules such as electrical, optical and conductivity properties. Specifically, the selection of metals such as Tin (Sn) may offer unique chemical structure and properties that could potentially lead to enhance energy storage devices performance such as batteries. In this work, the synthesis of $(NH_4)_2SnCl_6$ as cathode material for Li-ion batteries was carried out following a simple chemical precipitation method. The material was characterized by X-ray diffraction to analyze the crystallographic structure and SEM to analyze the morphology of the active compound also, IR spectrum was recorded. The inorganic-organic material was tested in a CR2032 coin cell configuration and its electrochemical properties were measured. Cyclic voltammetry was used to analyze the oxidation-reduction phenomena, several features were observed within a voltage range from 0.01 to 2V Discharge/charge process were investigated. The obtained discharge capacity was close to 160 $mAhg^{-1}$ at 20 mAg^{-1}.

1. Introduction

Perovskite structure compounds have attracted the attention since they are suitable materials for their application in solar cells being the lead-based perovskites, such as $PbTiO_3$ and $PbZrO_3$, some of most promising compounds for this purpose.[1] Their use is not limited to energy production also, lead perovskites can be used as cathode materials in energy storage devices. [2,3] Their high ionic conductivity and structural stability make them suitable candidates for improving battery performance and extending cycle life. Despite their advantages, there is a challenge, lead is a toxic element, and its use in batteries raises environmental and health concerns.[4] Therefore, it is highly desirable to find high-efficiency, low-cost and environment-friendly alternatives. Research is focusing on mitigating these issues exploring lead-free perovskite alternatives[5,6,7,8]. Non-metallic ion batteries have shown their competitiveness and promise to replace metal ion systems incorporating organic ions.[9] As an example, ammonium hexachlorometallates, which are complex compounds with the general formula $(NH_4)_2XCl_6$ (where X = metal), have emerged as an alternative to lead perovskites due to their notable crystalline structure and high stability.[10] For example, the compound NH_4FeF_3 has been proposed as potential material for energy storage. This material was observed to have a significant performance in lithium-ion batteries. Its theoretical capacity (206 $mAhg^{-1}$) was achieved at a current rate of C/2 with a capacity retention of 94% after 100 cycles.[11] Moreover, ammonium vanadates[12, 13] (e.g. $NH_4V_4O_{10}$, $NH_4V_3O_8{\cdot}2.9H_2O$, $(NH_4)_2V_{10}O_{25}{\cdot}8H_2O$) have been reported for energy storage and exhibit good electrochemical performance, being the $NH_4V_4O_{10}$ the compound that showed the highest specific capacity of 103 $mAhg^{-1}$ at 0.1 Ag^{-1}.

In this paper, we suggest a hybrid organic-inorganic $ASnCl_6$-based electrode (A = inorganic cation) for lithium-ion battery application, and an evaluation of its electrochemical capacity, as well as a reaction

mechanism proposed. The electrochemical capacity was evaluated by means of discharge-charge profiles, reaching a specific capacity of 160 $mAhg^{-1}$, with a capacity retention close to 95% in the 50th cycle at current density of 20 mAg^{-1}.

2. Materials and methods

2.1 Synthesis of $(NH_4)_2SnCl_6$

$(NH_4)_2SnCl_6$ powder was prepared by dissolving 1 mmol $SnCl_4{\cdot}5H_2O$ (Sigma-Aldrich, 99.8%) in 3.5 mL HCl solution (Sigma-Aldrich, 37%) with constant stirring at ambient condition. On the other hand, 2mmol NH_4Cl (CTR, 99.6%) was dissolved in 2.5 mL deionized water. The NH_4Cl solution was immediately dropped into the acid $SnCl_4$ solution. The mixture was stirred in a flask under reflux for 24h. Finally, the precipitate was extracted out from the crude solution via centrifugation at 5000 rpm for 5 min. Finally, the product was dried in a vacuum oven at 60°C for 24h.

2.2 Structural characterization.

The crystal structure study and phase identification of the obtained reaction product was carried out by X-ray diffraction (XRD) using a D2-Phaser, Bruker with Cu Kα radiation source (λ = 1.5418 Å). The scanning rate was 0.05°/s and analyzing within the angle range from 5 to 50°.

To analyze the morphology of $(NH_4)_2SnCl_6$ crystallites, SEM images were obtained by using a Neoscope JCM-6000 instrument from JEOL.

The infrared spectrum was recorded at room temperature, in 1000–3500 cm^{-1} spectral range with a 4 cm^{-1} resolution, by using a Interspec 200-X FT IR spectrometer. The $(NH_4)_2SnCl_6$ sample was ground in a clean mortar into fine powder, 1 mg of it was mixed and ground with KBr in order to make a 1mm thickness pellet by using an 8 t press.

2.3 Batteries fabrication.

Cathode fabrication: Active material [$(NH_4)_2SnCl_6$ powder], carbon black (Carbon Super P, TIMCAL) and Polytetrafluoroethylene (powder 35 μm particle size, Sigma-Aldrich) were taken in a 60:30:10 ratio (100 mg total dry weight per batch), and hand mixed to form a homogeneous powder. After that, two drops of isopropyl alcohol were added to allow the formation of a paste. The paste was roll-pressed and compressed on a 9 mm diameter stainless-steel mesh. The fabricated cathodes were dried for 24 hours at 60°C in a vacuum oven to remove moisture.

After drying, cathodes were transferred into a dry box (Omni-Lab 0210, VAC) filled with Argon (H_2O < 5 ppm).

Batteries assemble: Coin-type cells were assembled in an argon glove box to prevent moisture. A pure lithium foil was used as counter and reference electrode and the prepared cathode (described in cathode fabrication section) as the working electrode.[14] A microporous separator (Celgard 2325-1750-A) was included as separator. The electrolyte solution was prepared dissolving 1M $LiPF_6$ (Sigma Aldrich) in 1:1 volume ratio of ethylene carbonate (EC, Sigma Aldrich) and ethyl methyl carbonate (EMC, Sigma Aldrich) and stirring for 2h at room temperature.

2.4 Electrochemical Characterization.

Cyclic voltammetry (CV) curves were acquired through a MacPile II at scan rate of 125 μVs^{-1}. Charge/discharge probes were performed on a multichannel battery cycler BTS-4000 (Neware Electronic Co.) within the voltage range from 0.01 to 2 V at different current rates (from 20 mAg^{-1} to 800 mAg^{-1}).

3. Results and discussion

$(NH_4)_2SnCl_6$ possess a cubic structure belonging to the space group *Fm3̄m.* The structure contains Sn-centered undistorted $SnCl_6^{2-}$ octahedra with Sn–Cl distances of 2.429 Å, and tetrahedral NH^{4+} cations with N–H distances of 0.99 Å. The NH^{4+} cations have twelve Cl neighbors, three from each of four $SnCl_6^{2-}$ ions at 3.559 Å.[15]

Lithium atoms have an ionic radius close to 1 Å therefore, easier diffusion of lithium through $(NH_4)_2SnCl_6$ is possible.

X-ray diffraction was used to analyze the structure of powdered single crystals. $(NH_4)_2SnCl_6$ exhibits Fm3m Fig. 1 depicts the XRD pattern of the $(NH_4)_2SnCl_6$ sample compared to the cardboard number 9013381.[15] All the peaks matched to those corresponding for the cubic group space with cell parameters a = 9.9874 Å (± 0.07614) and V = 996.2252 (± 22.51) $Å^3$. [16]

To calculate crystallite size, Scherer Eq. 1[7], indicated in Eq. 1, was used.

$$D = K\lambda / \beta \cos\theta$$

1

where K is the Scherrer constant (for calculations, 0.9 was the accurate value), λ is the wavelength of the X-ray beam (0.154 nm), β is the Full Width at Half Maximum (FWHM) of the peak and θ is the Bragg angle. According to experimental data, the average size of crystallite was estimated in 25.65 nm.

The pattern is composed by several peaks at 2θ of 15.4°,17.7°, 25.3°, 29.6°, 30.9°, 35.7°, 39.1°, 40.2°, 44.3° and 47.2° which are assigned to the lattice planes (111), (200), (220), (311),(222), (400),(331), (420),(422) and (511), respectively which confirm the cubic structure of ammonium tin chloride (JCPDS 000070198).

Figure 2 depicts SEM images corresponding to the synthetized sample. The electron microscope images clearly show the presence of several particles with faces related to a cube structure. Figure 2a shows the agglomeration of these particles at a x400 magnification leading to the formation of large groups with a size less than 50 μm, no fractures or tunnels were observed in the matrix of the structures but in some particles the surface is eroded. Figure 2b reveals the presence of several particles at a x2000 magnification with the characteristic cube structure with a particle size not over passing the 50 μm limit. To extend our analysis of SEM images, Energy Dispersive X-ray (EDX) measurements were carried out, results are depicted in Fig. 2c.

EDX analysis indicates the presence of tin, chlorine and nitrogen, elements which match with our sample, the signals related to the presence of tin are low compared with those corresponding to chlorine, this might be due to the atomic relation of 6:1 of chlorine to tin in the anion $(SnCl_6)^{2-}$. Finally, the presence of aluminum is due to the use of an Al holder. Furthermore, energy-dispersive X-ray spectroscopy (EDX) mapping indicates a homogenous distribution of the elements (Cl, N, and Sn) within octahedral particles as observed in Fig. 3. Inside particles, areas of higher Cl concentration are found in the fully discharged samples followed by the presence of tin.

Additionally, to gain more information on the crystal structure, a vibrational study was conducted using infrared spectroscopy. The IR spectrum of this compound shows the characteristic signals of the NH_4^+ ion as shown in Fig. 3. The high-frequency regions between 3200 and 2800 cm^{-1} are attributed to the stretching vibrations of N-H organic groups. The vibration band at 1400 cm^{-1} is assigned to asymmetric bending vibrations of NH_4^+ and the peak located at 1200 cm^{-1} is assigned to ending vibration of NH_2. These assignments are in good agreement with those explained in literature. [18,19,20] Regarding the hexachlorostannate anion, the internal vibrational modes of $(SnCl_6)^{2-}$ anion would appear below 500 cm^{-1} in IR according to literature. [21]

Regarding the electrochemical characteristics of $(NH_4)_2SnCl_6$ perovskite, cyclic voltammetry profiles were recorded over a potential window from 0.01 to 2V and are depicted in Fig. 4a, several peaks are identified in the CV profiles. For the anodic region there are five peaks located at 0.49, 0.63, 0.74, 0.79 and 0.97 V vs. Li/Li+. All these features maintain their position on each cycle and might indicate the oxidation of $(NH_4)_2SnCl_6$. On the other hand, the cathodic region shows three peaks located at 0.3, 0.62 and 1.5 V related to the reduction of $(NH_4)_2SnCl_6$ and the release of lithium ions. After the second cycle, only the peak located at 0.3 V maintains its position and the remaining peaks disappear over time. The first observed anodic peak at 0.49 V and the cathodic peak at 0.3 V might be related with the removal and insertion of Li^+ ions into $(NH_4)_2SnCl_6$ structure, respectively. The cathodic peak at 1.5 V could be related to the formation of a solid-electrolyte interphase (SEI) since it disappears in the following cycles. During the positive scan, oxidation reactions occurred, removing the electrons and increasing the potential of the working electrode. When negative scan is running, reduction reactions could reduce the oxidation state of Sn atoms, favoring the decreasing of positive charges in the electrochemical device.

That way, the working electrode requires positively charged particles, such as Li^+ present into the electrolyte solution. Li^+ intercalates into the electrode to balance the charge. This process occurs, mainly at the surface of $(NH_4)_2SnCl_6$ since no tunnels or cavities were found in accordance with SEM images. Conversely, to overcome the excess charge, the crystal matrix requires the release of positively charged species into the electrolyte to return to the neutral state.

Further, batteries were subjected to galvanostatic cycling test to analyze their electrochemical capacity, discharge and charge capacity profiles were measured varying the charge rate from 20 mAg^{-1} to 500 mAg^{-1} as indicated in Fig. 4b. Discharge capacities of 160, 100, 60, 28 and 4 $mAhg^{-1}$ were obtained at 20, 50,100, 200 and 500 mAg^{-1}, respectively. According to the theoretical capacity of $(NH_4)_2SnCl_6$ (218 mAh/g), the efficiency of the electrochemical reaction is 73%.

Regarding charge capacities, the first cycle at 20 mAg^{-1} shows a charge capacity of 152 $mAhg^{-1}$, a value considerable close to the reported for discharge capacity at same rate. For subsequent charge profiles, the capacities are 97.7, 54.4, 27.7, 3.3 $mAhg^{-1}$ at 50, 100,200 and 500 mAg^{-1} respectively.

Cycle stability measurements were carried out to analyze reversible capacity of $(NH_4)_2SnCl_6$ at a current rate of 50 mAg^{-1}, the stability behavior is shown in Fig. 4c. According to our results, the $(NH_4)_2SnCl_6$-based cathode is capable of maintain around 50% of its initial capacity after 50 cycles with a capacity retention efficiency between 95%-99%. A slow capacity decay was observed in the first 20 cycles (at 20 mAg^{-1}) although the capacity retention efficiency is close to 100%. After 20th. cycle a progressive capacity decay was observed with some relevant points where capacity increases but then, it decreases strongly until the 40th. cycle, also fluctuations in the capacity retention efficiency are observed. Finally, for the last 10 cycles the capacity decreases reaching a value close to 80 $mAhg^{-1}$, half of its initial value. However, after 25 cycles, the retention efficiency becomes stable and reaches ≈ 100%, indicating that lithium ions shuttling became more or less reversible at this point. [22] The capacity detriment process might be related to the decomposition of $(NH_4)_2SnCl_6$ weaking the conductivity of the perovskite electrode. Subsequent increase of capacity might be correlated to the improvement of contact between the electrolyte solution and the electrode active material.[23,24]

To extend our understanding about the role of $(NH_4)_2SnCl_6$ as cathode in lithium-ion batteries, capacity measurements over a range of long cycles at different charge rates were performed, results are presented in Fig. 4d. Initially, the cathode exhibits a specific capacity within 160–170 $mAhg^{-1}$ range for the first ten cycles at 20mAg. The retained capacities of 120,40 and 9 $mAhg^{-1}$ when current increases from 50, 100, and 200 mAg were observed, respectively. When the current density comes back to 20 mAg the specific capacity of perovskite cathode almost recovered quickly close to 160 $mAhg^{-1}$. With increasing current rates, the $(NH_4)_2SnCl_6$ electrode delivered significantly decreasing capacities.

Additionally, batteries were tested over a current rate range from 20 to 100 mAg^{-1} for 50 cycles as presented in Fig. 4e. The comparison of our data shows that 20 mAg^{-1} is the optimal current density to perform measurements on the $(NH_4)_2SnCl_6$ cathode. Increasing the current rate promotes a decrease in the capacity. At higher current densities, the rate of lithium-ion movement within the electrolyte and across the electrode interfaces becomes a limiting factor. The ions may not be able to move quickly enough to keep up with the demand, leading to a reduced effective capacity as observed for the 50 and 100 mAg^{-1} rates.

To explore the morphological and structure stability of $(NH_4)_2SnCl_6$ material, we performed EDX and XRD measurements of postmortem cathodes. Figure 5a refers to an electron image from the region we explored, as observed, no evidence of the initial structure of $(NH_4)_2SnCl_6$ is maintained after cycling. Figure 5b-d indicates the distribution of oxygen, fluor and phosphorus, elements present in the electrolyte. The images show the well distribution of the electrolyte solution over the surface of the cathode. Figures 5e-f depict the distribution of chlorine and tin respectively. Both images show a non-uniform distribution of the elements and suggest that after cycling, the morphology and chemical composition are not retained suggesting the limited stability of $(NH_4)_2SnCl_6$.

To complete our analysis about the stability of $(NH_4)_2SnCl_6$, we performed X-ray measurements on cathodes after 50 cycles and compared it to pristine cathode results are posted in Fig. 7. It can be observed that Fig. 7a reveals the presence of those peaks corresponding to $(NH_4)_2SnCl_6$ material (marked with black asterisks) and peaks related to the stainless mesh used as support during the cathode fabrication (red asterisk). Figure 7b presents the XRD pattern of $(NH_4)_2SnCl_6$ cathode after cycling. It is important to observe that the peaks located at 2θ = 15.4° and 25.4° disappears after cycling, this might indicate a change on the structure due to the lithiation/delithiation processes and the formation of subproducts between the interaction of lithium with tin, the remaining peaks are still observable with less intensity. On the other hand, Fig. 7b demonstrates the presence of peaks located at 2θ = 23.9°,31.5° and 45.3°, their intensity is low but noticeable, these peaks are attributed to the formation of Li_xSn_y alloy.[25] Based on the results discussed, we have examined possible conversion reactions for Li and $(NH_4)_2SnCl_6$ based on the fundamental decomposition products observed by X-ray diffraction and voltammetry measurements which suggest that the reaction involved is irreversible. The proposed potential conversion reaction is divided in three steps; first, lithium intercalates between the available spaces in $(NH_4)_2SnCl_6$ as described in Eq. 1. Also, lithium is capable of reacting reactions with the organo-metallic perovskite leading to a conversion reaction as suggested by Eq. 2, reduction of tin might occur in two steps since several peaks were observed in the anodic region according to the cyclic voltammetry results. Finally, as XRD patterns of postmortem cathode suggest, Lithium forms an alloy with tin as indicated in Eq. 3 and it might be occurring in two steps since lithium is capable to form alloys with tin in distinct atomic relations.[26,27, 28]

$$xLi + (NH_4)_2SnCl_6 \rightarrow \quad Li_x(NH_4)_2SnCl_6 \qquad Eq.\ 1$$

$$4xLi + (NH_4)_2SnCl_6 \rightarrow Li_{2x}(NH_4)_2Sn_{1-x}Cl_{6-2x} + 2xLiCl + xSn \qquad Eq.\ 2$$

$$xLi + ySn \rightarrow Li_xSn_y \qquad Eq.\ 3$$

To demonstrate the feasibility of $(NH_4)_2SnCl_6$ as potential cathode in lithium-ion batteries, we compared previous reports about the use of similar ammonium-based compounds in batteries with the present work. Table 1 summarizes the discharge capacity of perovskite materials for lithium-based energy storage devices.

Table 1
Comparison between reported ammonium-based cathode materials and $(NH_4)_2SnCl_6$

Active material	Discharge Capacity $mAhg^{-1}$	Ion-battery	Reference
$NH_4V_4O_{10}$	103	Ammonium-ion	[13]
$(NH_4)_2V_7O_{16}$	89	Calcium-ion	[29]
$NH_4MnPO_4{\cdot}H_2O$	90	Zinc-ion	[30]
NH_4^+-rich nickel hexacyanoferrate	50.2	Ammonium-ion	[31]
$(NH_4)_2SnCl_6$	160	Lithium-ion	This work

As observed, the $(NH_4)_2SnCl_6$ cathodes described in this research releases a moderate capacity higher than those ammonium-based materials.

Conclusion

In this study, a positive result was achieved for lithium-ion batteries by incorporating ammonium hexachlorostannate perovskite as active material in the cathode. It was discovered that $(NH_4)_2SnCl_6$ is a suitable material for energy storage since the outstanding capacity was about 160 $mAhg^{-1}$ with a high coulombic efficiency close to 95%, in this way, the use of $(NH_4)_2SnCl_6$ enables a new pathway for the development of cathode materials for LIBs based on the incorporation of organic-inorganic compounds.

Declarations

Author Contribution

Alfredo Romero executed most of the experiments and drafted the initial version of the manuscript. Thelma Serrano assisted with the in-depth analysis of SEM microscopy. Nora Garcia contributed to the description and analysis of the FTIR and electrochemical experiments. Salome de la Parra assisted in

the execution and description of the X-ray diffraction experiments. Eduardo Sanchez, as the project leader, contributed the original idea for the project and supervised its execution. All authors participated in the writing and revision of the final manuscript.

Acknowledgment

Authors acknowledge to Consejo Nacional de Humanidades, Ciencias y Tecnologías, CONAHCyT, Mexico for finnacial suppport. A. Romero- Contreras acknowledges CONAHCyT the invaluable opportunity granted through the postdoctoral fellowship 2023.

References

1. Chaupatnaik, A., & Barpanda, P. (2021). Perovskite lead-based oxide anodes for rechargeable batteries. *Electrochemistry Communications*, *127*, 107038. https://doi.org/10.1016/j.elecom.2021.107038
2. Kostopoulou, A., Vernardou, D., Savva, K., & Stratakis, E. (2019). All-inorganic lead halide perovskite nanohexagons for high performance air-stable lithium batteries. *Nanoscale*, *11*(3), 882-889. https://doi.org/10.1039/c8nr10009h
3. Wang, Q., Yang, T., Wang, H., Zhang, J., Guo, X., Yang, Z., Lu, S., & Qin, W. (2019). Morphological and chemical tuning of lead halide perovskite mesocrystals as long-life anode materials in lithium-ion batteries. *CrystEngComm*, *21*(6), 1048-1059. https://doi.org/10.1039/c8ce01779d
4. Chen, P., Qi, J., Klug, M. T., Dang, X., Hammond, P. T., & Belcher, A. M. (2014). Environmentally responsible fabrication of efficient perovskite solar cells from recycled car batteries. *Energy & Environmental Science*, *7*(11), 3659-3665. https://doi.org/10.1039/c4ee00965g
5. Yang, S., Liang, Q., Wu, H., Pi, J., Wang, Z., Luo, Y., Liu, Y., Long, Z., Zhou, D., Wen, Y., Wang, Q., Guo, J., & Qiu, J. (2022). Lead-Free Double Perovskite Cs2NaErCl6: Li+ as High-Stability Anodes for Li-Ion Batteries. *The Journal Of Physical Chemistry Letters*, *13*(22), 4981-4987. https://doi.org/10.1021/acs.jpclett.2c01052
6. Pandey, P., Sharma, N., Panchal, R. A., Gosavi, S. W., & Ogale, S. (2019). Realization of High Capacity and Cycling Stability in Pb-Free A2CuBr4 (A=CH3NH3/Cs, 2 D/3 D) Perovskite-Based Li-Ion Battery Anodes. *ChemSusChem*, *12*(16), 3742-3746. https://doi.org/10.1002/cssc.201900959
7. Ch, L. T. L., Medina, A., Jaramillo, F., Calderón, J. A., Lavela, P., & Tirado, J. L. (2023b). New insights on the reaction mechanism and charge contribution of NaNiF3 perovskite as an anode for sodium-ion batteries. *Electrochimica Acta*, *453*, 142341. https://doi.org/10.1016/j.electacta.2023.142341
8. López, L. T., Ramírez, D., Jaramillo, F., & Calderón, J. A. (2020). Novel hybrid organic-inorganic CH3NH3NiCl3 active material for high-capacity and sustainable lithium-ion batteries. *Electrochimica Acta*, *357*, 136882. https://doi.org/10.1016/j.electacta.2020.136882
9. Xu, G., Nie, P., Dou, H., Ding, B., Li, L., & Zhang, X. (2017). Exploring organic metal frameworks for energy storage in batteries and supercapacitors. *Materials Today*, *20*(4), 191-209.

https://doi.org/10.1016/j.mattod.2016.10.003

10. Pelzl, J., & Dimitropoulos, C. (1994). Effect of Deuteration on the Phase Transitions and on the Critical Dynamics in Ammonium Hexachlorometallates. *Zeitschrift Für Naturforschung A*, *49*(1-2), 232-246. https://doi.org/10.1515/zna-1994-1-235
11. Martin, A., Santiago, E. S., Kemnitz, E., & Pinna, N. (2019). Reversible Insertion in AFeF3 (A = K+, NH4+) Cubic Iron Fluoride Perovskites. *ACS Applied Materials & Interfaces*, *11*(36), 33132-33139. https://doi.org/10.1021/acsami.9b10659
12. Wang, P., Zhang, Y., Jiang, H., Dong, X., & Meng, C. (2022). Ammonium vanadium oxide framework with stable NH_4^+ aqueous storage for flexible quasi-solid-state supercapacitor. *Chemical Engineering Journal*, *427*, 131548. https://doi.org/10.1016/j.cej.2021.131548
13. Zheng, J., Zhang, Y., Hu, T., Lv, T., & Meng, C. (2018). New Strategy for the Morphology-Controlled Synthesis of V_2O_5 Microcrystals with Enhanced Capacitance as Battery-type Supercapacitor Electrodes. *Crystal Growth & Design*, *18*(9), 5365-5376. https://doi.org/10.1021/acs.cgd.8b00776
14. Jache, B., Mogwitz, B., Klein, F., & Adelhelm, P. (2013). Copper sulfides for rechargeable lithium batteries: Linking cycling stability to electrolyte composition. *Journal Of Power Sources*, *247*, 703-711. https://doi.org/10.1016/j.jpowsour.2013.08.136
15. Demartin, F., Campostrini, I., & Gramaccioli, C. M. (2009). Panichiite, natural ammonium hexachlorostannate(IV), $(NH_4)_2SnCl_6$, From La Fossa Crater, Vulcano, Aeolian Islands, Italy. *The Canadian Mineralogist*, *47*(2), 367-372. https://doi.org/10.3749/canmin.47.2.367
16. Lerbscher, J. A., & Trotter, J. (1976). Potassium hexachlorostannate(IV) and ammonium hexachlorostannate(IV). *Acta Crystallographica Section B*, *32*(9), 2671-2672. https://doi.org/10.1107/s0567740876008480
17. Thomas, S., Kalarikkal, N., & Abraham, A. R. (2021). *Design, Fabrication, and Characterization of Multifunctional Nanomaterials*. Elsevier.
18. Mkaouar, I., Karâa, N., Hamdi, B., & Zouari, R. (2016). Synthesis, crystal structure, thermal analysis, vibrational study dielectric behaviour and Hirshfeld surface analysis of [C6H10(NH3)2)]2 SnCl6 (Cl)2. *Journal Of Molecular Structure*, *1115*, 161-170. https://doi.org/10.1016/j.molstruc.2016.02.070
19. Billing, D. G., Lemmerer, A., & Rademeyer, M. (2007). Bis(1-phenylethylammonium) hexachloridostannate(IV) and bis(2-phenylethylammonium) hexachloridostannate(IV). *Acta Crystallographica Section C Crystal Structure Communications*, *63*(3), m101-m104. https://doi.org/10.1107/s0108270107004970
20. Ertl, A., Hughes, J. M., Pertlik, F., Foit, F. F., Wright, S. E., Brandstatter, F., & Marler, B. (2002). POLYHEDRON DISTORTIONS IN TOURMALINE. *The Canadian Mineralogist*, *40*(1), 153-162. https://doi.org/10.2113/gscanmin.40.1.153
21. Mathlouthi, M., Valkonen, A., Rzaigui, M., & Smirani, W. (2016). Structural characterization, spectroscopic, thermal, AC conductivity and dielectric properties and antimicrobial studies of

(C8H12N)2[SnCl6]. *Phase Transitions*, *90*(4), 399-414. https://doi.org/10.1080/01411594.2016.1212194

22. Xiao, J., Li, Q., Bi, Y., Cai, M., Dunn, B., Glossmann, T., Liu, J., Osaka, T., Sugiura, R., Wu, B., Yang, J., Zhang, J., & Whittingham, M. S. (2020). Understanding and applying coulombic efficiency in lithium metal batteries. *Nature Energy*, *5*(8), 561-568. https://doi.org/10.1038/s41560-020-0648-z
23. Xu, Q., Ding, R., Shi, W., Ying, D., Huang, Y., Yan, T., Gao, P., Sun, X., & Liu, E. (2019). Perovskite $KNi_{0.1}Co_{0.9}F_3$ as a pseudocapacitive conversion anode for high-performance nonaqueous Li-ion capacitors and dual-ion batteries. *Journal Of Materials Chemistry. A*, *7*(14), 8315-8326. https://doi.org/10.1039/c9ta00493a
24. Qin, Y., Li, Q., Xu, J., Wang, X., Zhao, G., Liu, C., Yan, X., Long, Y., Yan, S., & Li, S. (2017). CoO-Co nanocomposite anode with enhanced electrochemical performance for lithium-ion batteries. *Electrochimica Acta*, *224*, 90-95. https://doi.org/10.1016/j.electacta.2016.12.040
25. Li, S., Wang, C., Yu, J., Han, Y., & Lu, Z. (2018). Understanding the role of conductive polymer in thermal lithiation and battery performance of Li-Sn alloy anode. Energy Storage Materials, 20, 7-13. https://doi.org/10.1016/j.ensm.2018.11.030
26. Dawson, J. A., Naylor, A. J., Eames, C., Roberts, M., Zhang, W., Snaith, H. J., Bruce, P. G., & Islam, M. S. (2017). Mechanisms of Lithium Intercalation and Conversion Processes in Organic–Inorganic Halide Perovskites. *ACS Energy Letters*, *2*(8), 1818-1824. https://doi.org/10.1021/acsenergylett.7b00437
27. Vicente, N., Bresser, D., Passerini, S., & Garcia-Belmonte, G. (2018). Probing the 3-step Lithium Storage Mechanism in CH3NH3PbBr3 Perovskite Electrode by Operando-XRD Analysis. *ChemElectroChem*, *6*(2), 456-460. https://doi.org/10.1002/celc.201801291
28. Vicente, N., & Garcia-Belmonte, G. (2017). Methylammonium lead bromide perovskite battery anodes reversibly host high Li-Ion concentrations. *The Journal Of Physical Chemistry Letters*, *8*(7), 1371-1374. https://doi.org/10.1021/acs.jpclett.7b00189
29. Wu, X., Liu, G., Yang, S., Li, Y., Wang, H., Li, Q., & Wu, X. (2022). Hydrated ammonium manganese phosphates by electrochemically induced manganese-defect as cathode material for aqueous zinc ion batteries. *Chinese Chemical Letters*, 34(4), 107540. https://doi.org/10.1016/j.cclet.2022.05.054
30. Zhang, P., Zhang, X., Liu, D., Xiang, A., Lu, J., Jiang, Y., Yang, Z., & Hu, P. (2023). One Pot Synthesis of Ammonium Rich Nickel Hexacyanoferrate as Stable Cathode Material for Ammonium-Ion Batteries. *Batteries & Supercaps*, 7(3). https://doi.org/10.1002/batt.202300546
31. Bu, H., Lee, H., Hyoung, J., Heo, J. W., Kim, D., Lee, Y. J., & Hong, S. (2023). (NH4)2V7O16 as a Cathode Material for Rechargeable Calcium-Ion Batteries: Structural Transformation and Co-Intercalation of Ammonium and Calcium Ions. *Chemistry Of Materials*, 35(19), 7974-7983. https://doi.org/10.1021/acs.chemmater.3c01207

Figures

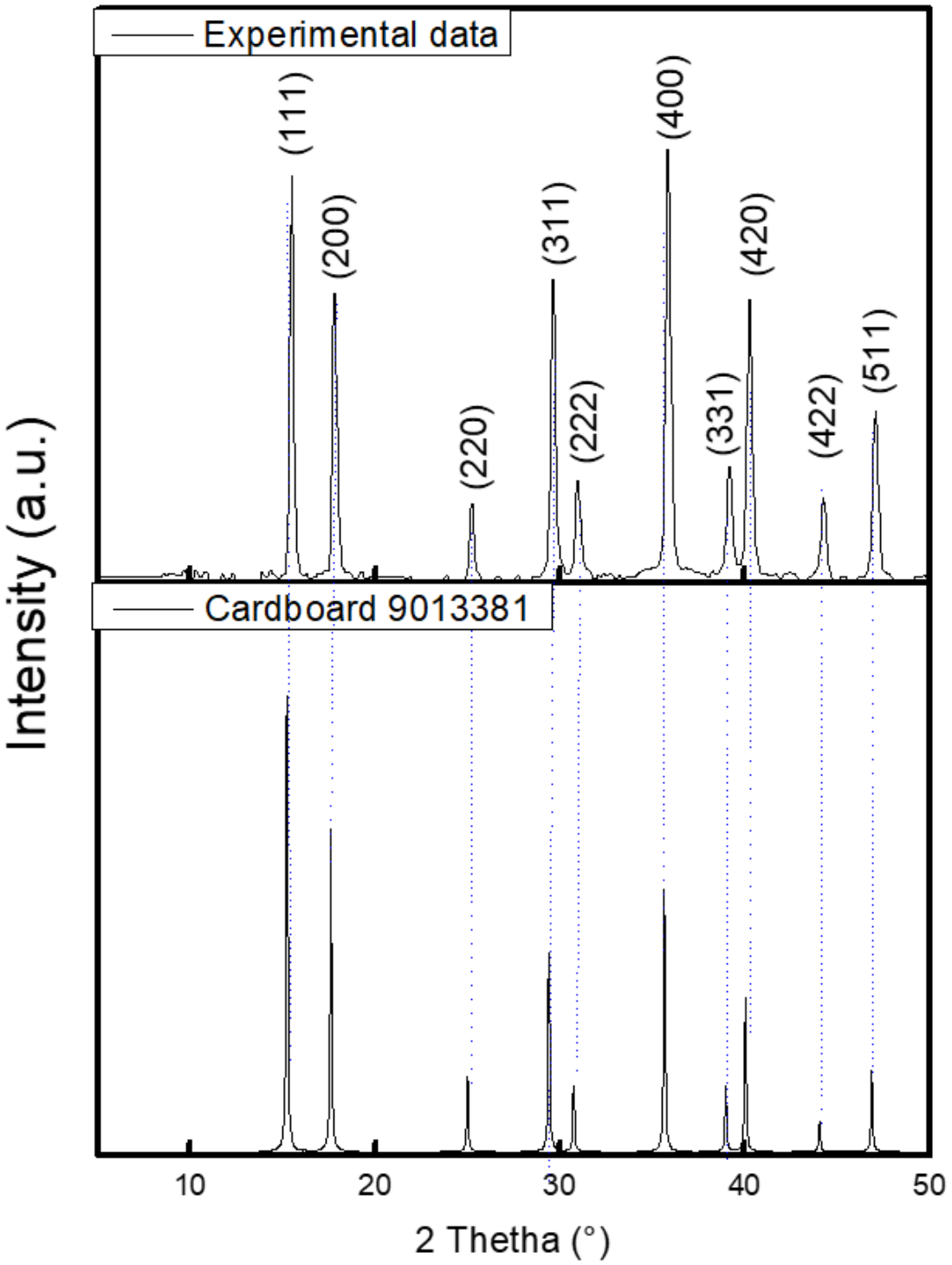

Figure 1

XRD patterns of pristine $(NH_4)_2SnCl_6$. The standard pattern of $(NH_4)_2SnCl_6$ (Cardboard 1010225) is also depicted as reference.

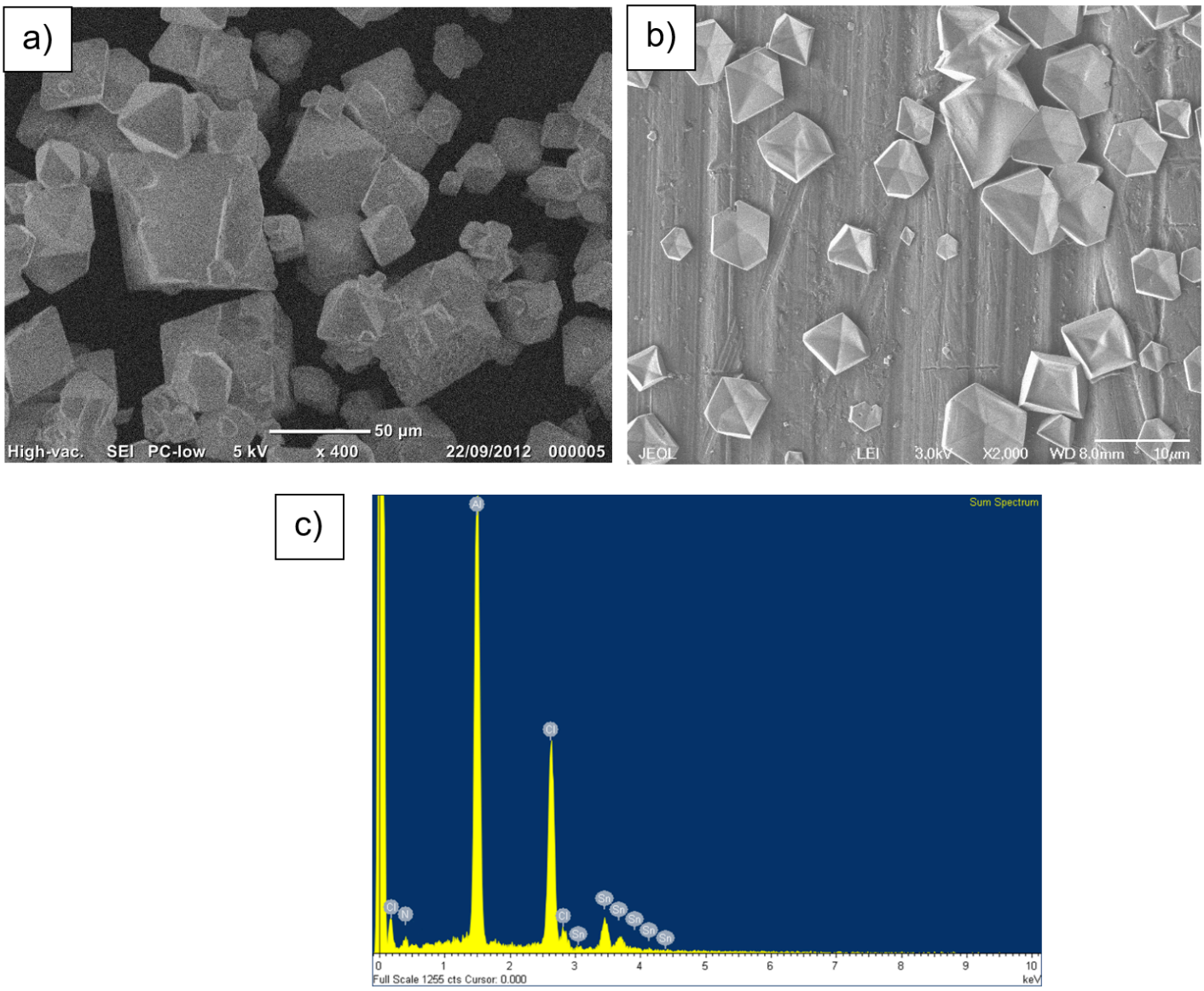

Figure 2

Morphology of the $(NH_4)_2SnCl_6$ crystallites observed by SEM: a) x400 magnification and b) x2000 magnification. c) EDX of synthetized sample.

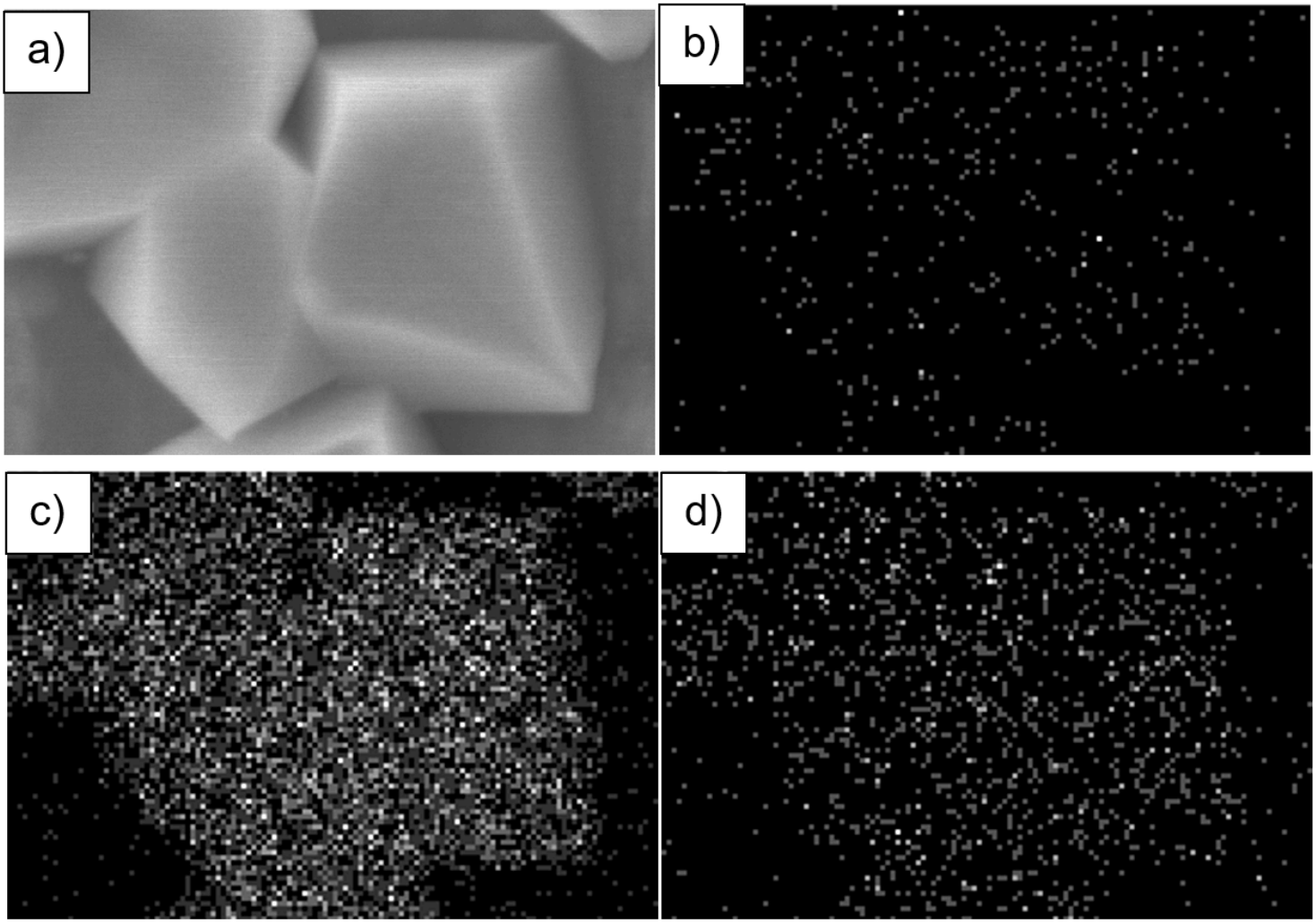

Figure 3

Elemental analysis of $(NH_4)_2SnCl_6$. a) Electron image, b) Nitrogen distribution, c) chlorine presence and d) tin mapping.

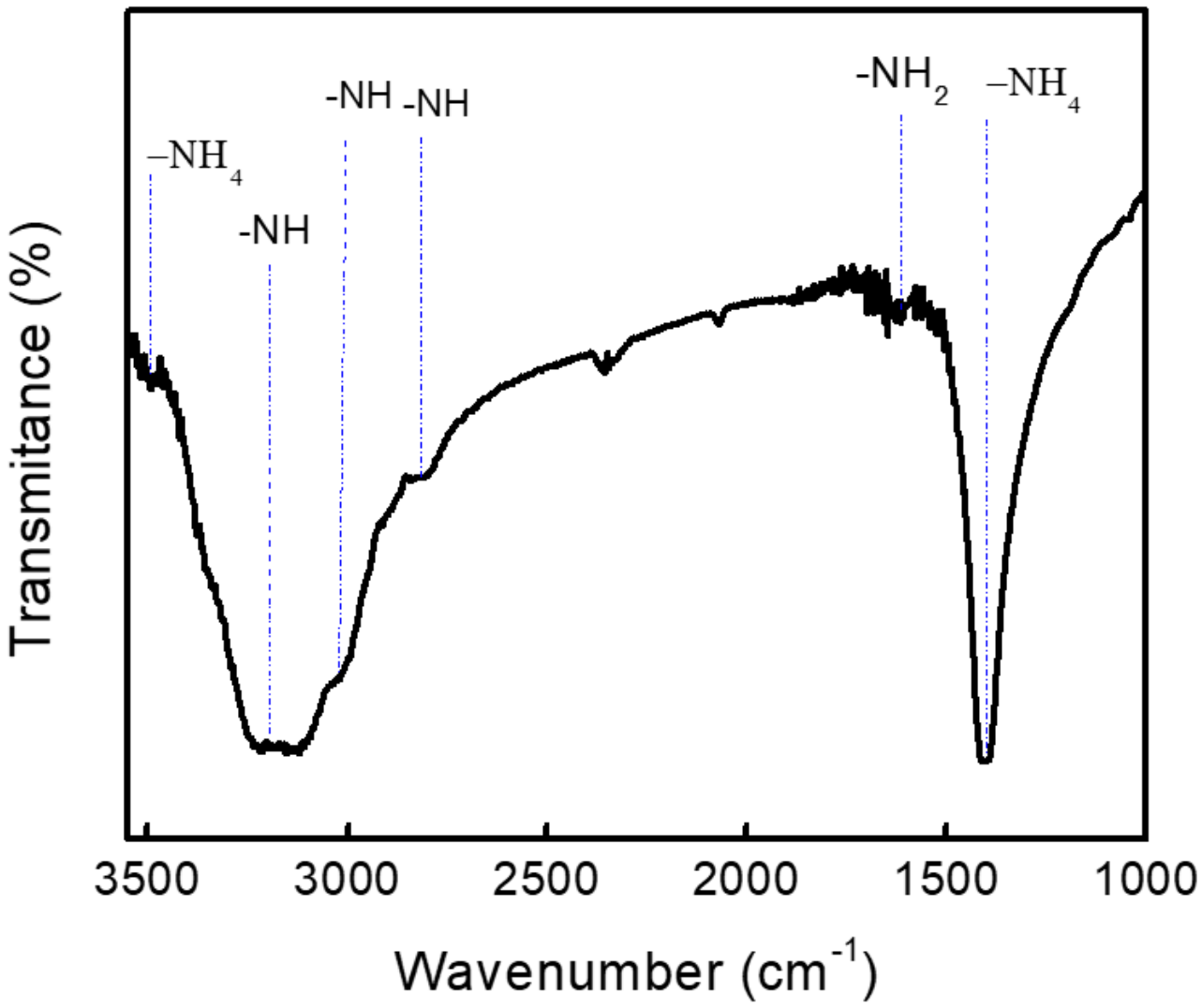

Figure 4

IR spectra of $(NH_4)_2SnCl_6$. Bands corresponding to the vibrational modes of Ammonium ion are identified.

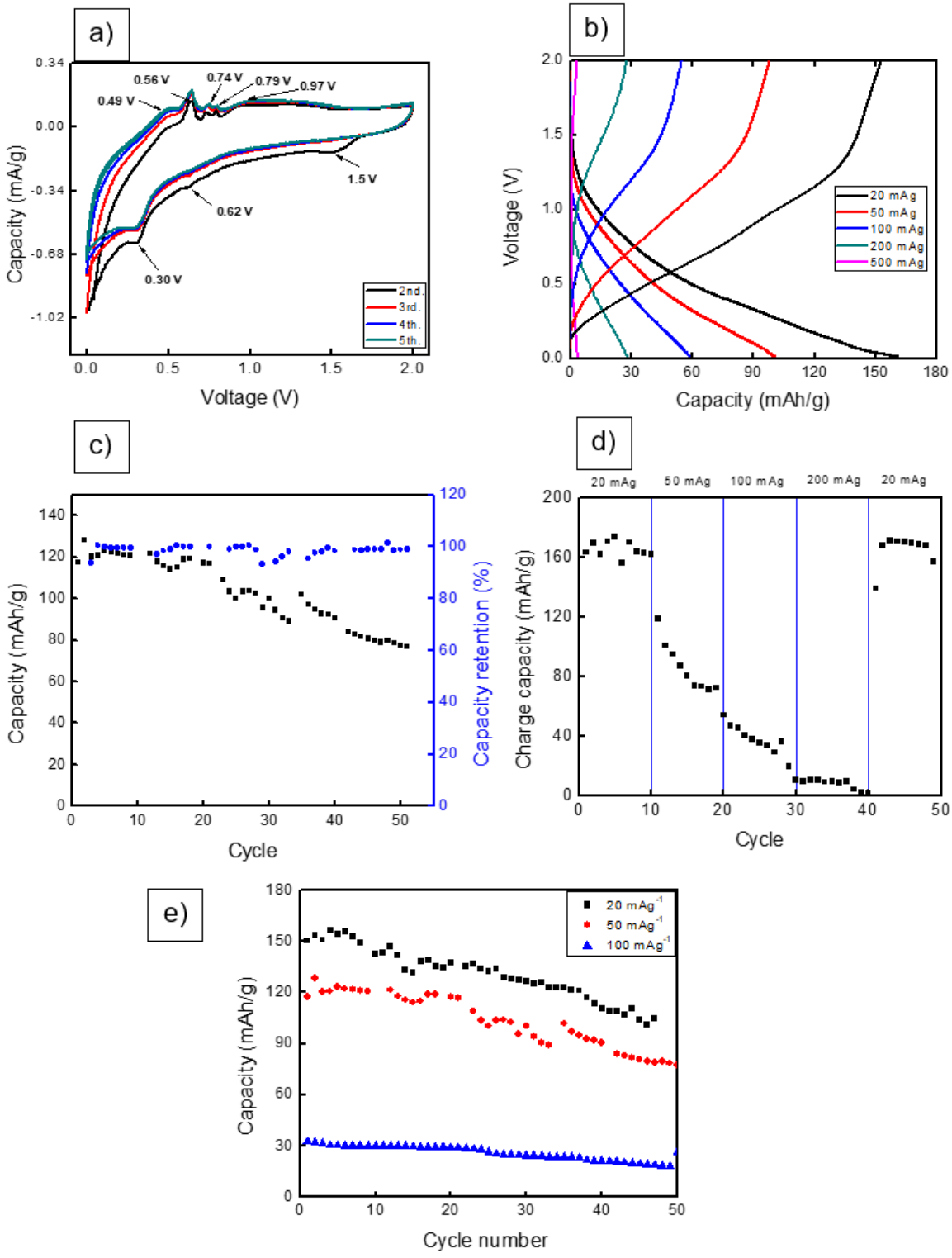

Figure 5

a) Cyclic voltammetry curves of the $(NH_4)_2SnCl_6$ compound at 0.125 μV/s rate. b) Discharge profiles for $(NH_4)_2SnCl_6$ at 20,50,100, 200, and 500 mAg, c) Cycle stability and coulombic efficiency of $(NH_4)_2SnCl_6$ at a current rate of 50 mAg within the voltage range of 0.01-2 V, d) Rate capability of $(NH_4)_2SnCl_6$ (discharge) electrodes at various current densities ranging from 20 mAg to 200 mAg.e) Cycle stability of synthetic compound at current rate of 20 mAg, 50 mAg and 100 mAg.

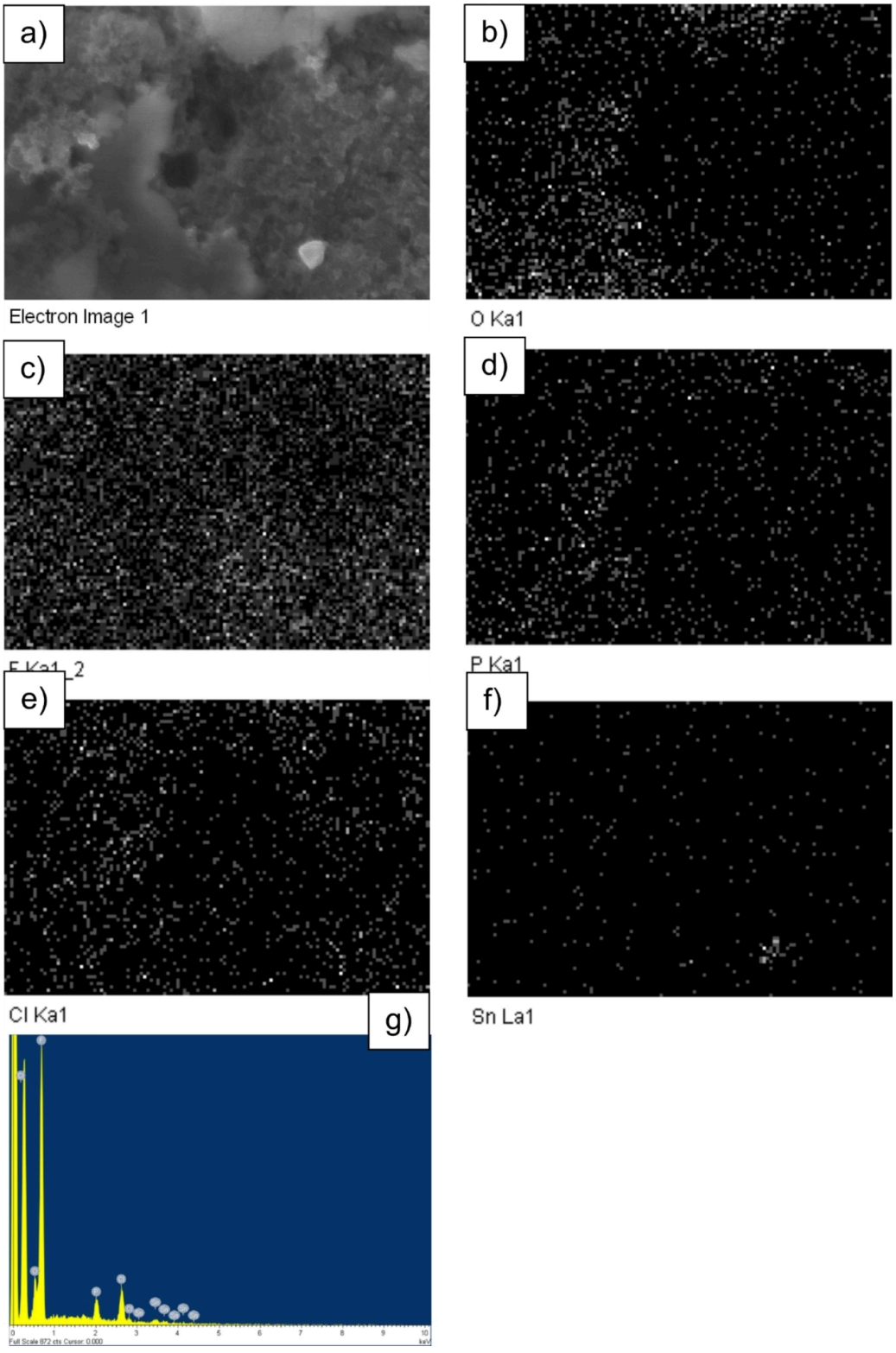

Figure 6

Elemental analysis of postmortem $(NH_4)_2SnCl_6$ cathode. a) Electron image, b) Oxygen distribution, c) fluor presence, d) phosphorus distribution, e) chlorine mapping f) tin presence and g) EDX measurement.

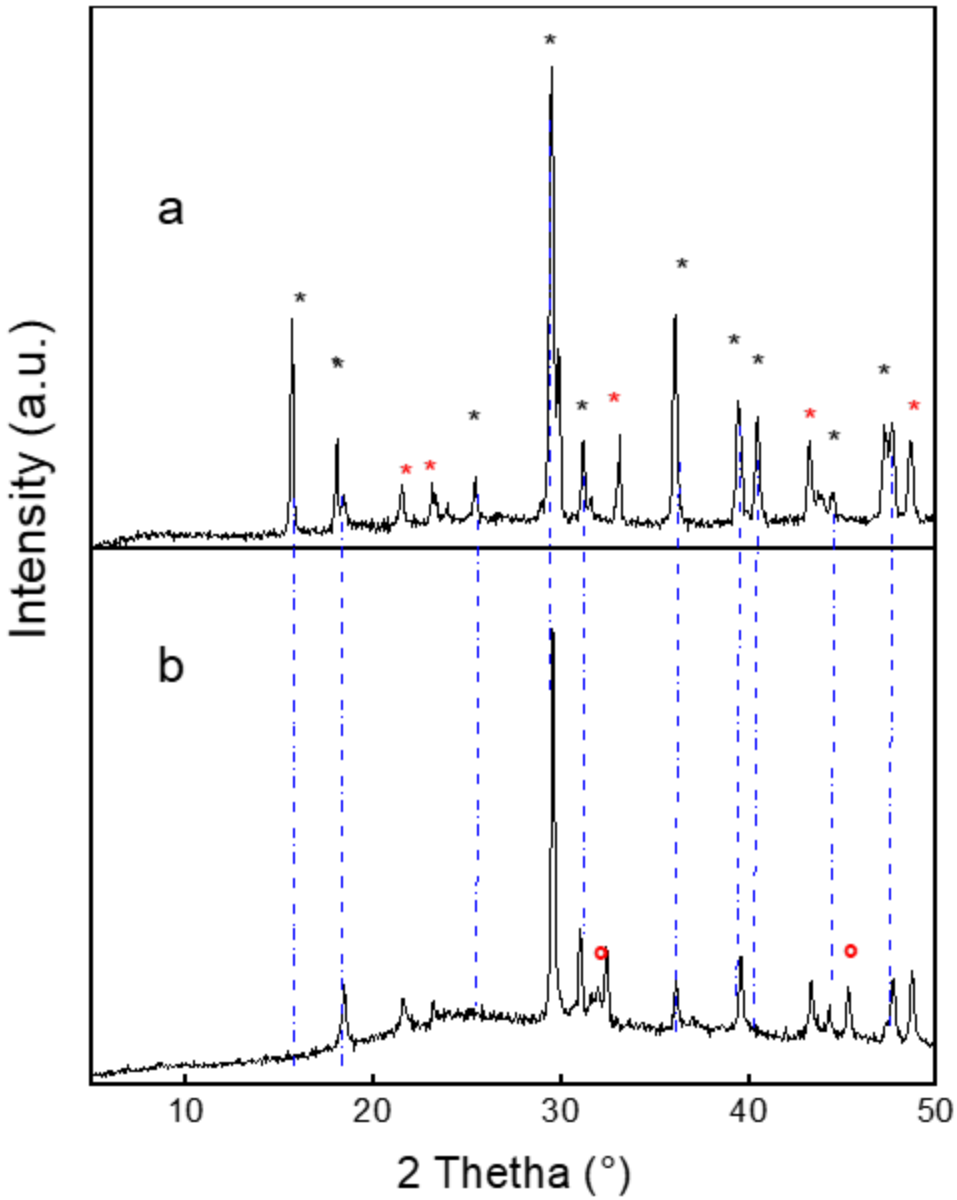

Figure 7

X-ray diffraction patterns corresponding to the prepared cathode a) before their incorporation in lithium-ion batteries and b) after 50 cycles. The black asterisk (*) indicates the peaks identified for the presence of $(NH_4)_2SnCl_6$ material, red asterisk (*) indicates the peaks corresponding to the stainless-steel mesh. Red circles (°) are to identify the peaks related to the possible formation of Li-Sn alloy.